SAND89-1692C

APPLICATION OF THE IFCI INTEGRATED FUEL-COOLANT INTERACTION CODE TO A FITS-TYPE POURING MODE EXPERIMENT*

by

Michael F. Young
Theory and Analysis Division
Sandia National Laboratories
Albuquerque, NM 87185

SAND--89-1692C

DE89 015392

ABSTRACT

The phenomenon of molten fuel-coolant interaction (FCI) is of considerable interest in many industrial processes where hot molten material may come in contact with water, including the pulp and paper, aluminum, steel, and nuclear power industries. The nature of the FCIs can range from mild film boiling, through energetic boiling, up to a violent vapor explosion. In the nuclear power industry, FCIs are of interest because of their possible consequences during hypothetical light water reactor core meltdown accidents. These interactions may occur under a variety of conditions either within the reactor vessel or in the reactor cavity. The IFCI computer code is being developed to investigate the FCI problem at large scale using a two-dimensional, four-field hydrodynamic framework and physically based models. IFCI will be capable of treating all major FCI processes in an integrated manner. The hydrodynamic method and physical models used in IFCI are discussed. Results from a test problem simulating a generic pouring mode experiment are presented.

1 Introduction

The phenomenon of molten fuel-coolant interaction (FCI) is of considerable interest in many industrial processes where hot molten material may come in contact with water, including the pulp and paper, aluminum, steel, and nuclear power industries. The nature of the FCIs can range from mild film boiling, through energetic boiling, up to a violent vapor explosion. The vapor explosion is the type of FCI of most interest, due to its industrial safety consequences. Vapor explosions have been involved in several industrial accidents, resulting in property damage, injury to workers, and loss of life. In the nuclear power industry, FCIs are of interest because of their effect on severe reactor accident scenarios, which are of importance to reactor licensing. FCIs can affect the course of severe reactor accidents through possible physical damage to the reactor vessel or containment building, dispersal of core materials, and steam and hydrogen production.

---

*This work was supported by the United States Nuclear Regulatory Commission, the Department of Energy, and the Department of Defense and was performed at Sandia National Laboratories, which is operated for the U.S. Department of Energy under contract number DE-AC04-76DP00789.

---

2 Background

2.1 FCI Processes

It is generally agreed that the FCI process can be roughly divided into four phases: the initial coarse mixing phase, the trigger phase, the detonating propagation phase, and the hydrodynamic expansion phase. These four phases are useful conceptually, although in reality they may all be occurring simultaneously in different spatial locations in the melt-coolant mixture region. The first three phases are also related to the various forms of FCI, in that the coarse mixing phase characterizes an FCI which involves only mixing and rapid boiling, the trigger phase represents an FCI wherein a local explosion occurs but does not propagate through the majority of the fuel-coolant mixture, and the propagation phase occurs in the propagating detonation form of FCI.

In addition to the four phases, there are also different contact modes that must be considered: the pouring mode, in which a mass of molten material is dropped into a pool of coolant; jet mixing, where a jet of melt is injected into coolant; and the stratified mode, where the melt is in a pool or layer, covered by a layer of coolant.

Coarse mixing is characterized by entry of molten material (melt) into a coolant (water) with accompanying vapor generation, intermixing of the melt, water, and vapor, and breakup of the melt into smaller diameter drops, (smaller meaning of order 0.1-10 cm); this phase occurs on a timescale of 0.1-1.0 s. During this phase, the melt and water are insulated from one another by a vapor film, which serves to maintain the fuel temperature close to its initial value throughout coarse mixing. Breakup of the melt is thought to be governed by hydrodynamic instabilities, notably the Rayleigh-Taylor and Kelvin-Helmholtz instabilities. These breakup processes are driven by relative velocity differences or accelerations between the melt and the water and steam.

Triggering occurs when some local disturbance collapses the vapor films around the melt; this collapse allows direct water-melt contact or near contact, high heat transfer rates to the water, and high relative velocities in the vicinity of the trigger. If the triggering event is sufficiently strong, the mixture may enter a detonating propagation phase. Triggering is not well understood, but is typically observed to occur quickly, on a timescale of around 100 μs, and is often initiated by contact of the melt with a solid surface.[1,2,3,4]

The explosive propagation phase is characterized by a "reaction zone" which propagates through the mixture region; within this reaction zone, the coarsely mixed melt is rapidly fragmented into particles in the 10-1000 μm size, with accompanying rapid increase in melt surface area, release of heat to the water and generation of shock waves. Typical experimentally observed propagation speeds are in the 50-500 m/s range.[5,6] The same hydrodynamic instabilities operative during coarse mixing could also be responsible for the rapid fine fragmentation occurring during propagation, although other mechanisms also may be operative (for instance, jet penetration of the melt by the water[7] or shock-wave induced fragmentation).

In the expansion phase, the expanding steam-water-melt mixture converts

thermal energy into work on the surroundings. This phase has been treated in detail by various researchers.[8,9,10]

2.2 Previous FCI Modeling

Past research on FCI phenomena has been both experimental and theoretical in nature, but has not totally succeeded in resolving questions on FCI effects at large scale. In general, most of this research has been directed to answer questions of reactor safety. Separate effects and integrated experiments have been performed at small and intermediate scales to investigate many FCI phenomena. These experiments have provided much useful information, but must, because of cost, be much smaller than actual reactor or industrial scales; FCIs have demonstrated scale-dependence in past experiments (for instance, the "pint theory"[5] lower limit on the amount of melt necessary for an FCI), and there are very likely other scale-dependent processes in FCIs that are unknown at this time, making the extrapolation of experimental data to industrial scale very uncertain. On the theoretical side, lack of data on basic FCI phenomena makes choosing the correct model from among competing models very difficult; without an accurate model of the physical phenomena occurring during an FCI, the experimental results cannot be confidently extended to large scale.

Early models and correlations tended to be parametric and address only isolated aspects of FCIs. As more knowledge on FCIs was gained, models evolved in the direction of including more physics; simultaneously, advances in computational hydrodynamics allowed incorporation of the more refined models in a suitable hydrocode framework, allowing more aspects of the FCI to be treated simultaneously in an integrated fashion.

These modeling efforts with hydrocodes have also evolved from simple models and one-dimensional, single field hydrocodes towards more physical models and two-dimensional, multifield hydrocodes. This evolution has taken place both as the limitations of early modeling efforts were recognized and as more advanced computational hydrodynamic techniques have become available.

Recent FCI modeling efforts have generally been aimed at either the coarse mixing phase or the detonation phase. Examples of coarse mixing calculations are those done by Bankoff et al.,[11] Abolfadl and Theofanous,[12] Thyagaraja and Fletcher,[13] and Chu and Corradini,[14] all for mixing in the lower plenum of a power reactor. Examples of propagation calculations are those of Carachalios et al.,[15] Medhekar et al.,[16] and Fletcher and Thyagaraja.[17] The above efforts generally have made simplifying assumptions, either in the hydrodynamic model or in the models of FCI phenomena, to make the problem more tractible. Several of the coarse mixing calculations, for instance, use a constant initial particle size,[11,12,13] an assumption that causes early high steam generation rates and consequent early separation of melt and coolant. The propagation calculations mentioned above are one-dimensional.

3 Objective of Paper

The IFCI[1] (Integrated Fuel-Coolant Interaction) computer code is being developed to investigate FCIs in as mechanistic a manner as possible. The code is intended to address all aspects of FCI phenomena, including coarse fragmentation and mixing of molten material with water, triggering, propagation and fine fragmentation, and expansion of the melt-water-steam system. The

ultimate objective of the code is to predict rates of steam and hydrogen generation, melt fragmentation and dispersion, fission product release, shock wave generation and propagation, and system loading for explosive and non-explosive FCIs in a reactor system.

This paper describes the current state of development of the IFCI code, the hydrodynamic model used, and the key models used to describe FCI phenomena, notably the dynamic fragmentation, surface area transport, subcooled boiling, and surface tracking models. The results of a test problem, simulating a generic pouring mode FCI experiment in the Fully Instrumented Test Series, or FITS,[5,7] are presented. This calculation served three main purposes: a demonstration that the code architecture is essentially complete and functional; an early qualitative assessment of the validity of the underlying models and constitutive relations; and an improved perspective on the needs for and priorities of further model development and experimental data.

4 IFCI Features

4.1 General Description

IFCI is based on a two-dimensional, four-field version of the SETS[18,19] hydrodynamic method. Use of a multifield method with separate mass, momentum, and energy equations for each field allows slip between the various materials (vapor, liquid coolant, and liquid melt; the fourth field, solid particulate, is not used in the present calculation), and a different temperature for each material. IFCI uses the TRAC equation of state[20] for water and steam (obtained by fits to the steam tables) and a stiff gas equation of state for the melt. The constitutive relations required for the interfield coupling terms (heat transfer, momentum exchange, and phase change) include a bulk boiling model, a subcooled surface boiling model, a three-field flow regime map, and adaptations of standard heat transfer and momentum transfer correlations.

Additional models are included which are necessary to calculate phenomena that occur in FCIs. These are: (1) a dynamic fragmentation model, which calculates the breakup, or change in effective diameter, of the melt based on local hydrodynamic conditions (densities and velocities), coupled with (2) a convection equation for melt surface area per unit volume; (3) a surface tracking model to follow the melt-coolant interface and, in particular, to calculate the melt characteristic length changes produced by large-scale (greater than finite-difference cell size) hydrodynamic motion of the melt; (4) a trigger model, to simulate a local explosion in a melt-water-steam mixture; (5) a melt oxidation/hydrogen production model; and (6) a detonation-fine fragmentation model to calculate the rapid fragmentation and steam generation in a propagating reaction zone. It appears, based on current understanding of FCIs, that these are the basic models necessary to calculate FCI phenomena; they may need to be supplemented later, as additional effects are discovered, but a code with these basic models should be capable of doing an adequate simulation of FCIs. IFCI presently includes models (1-5); (6) is under development.

4.2 Hydrodynamic Equation Set

The equation set used in IFCI is a four-field, two-dimensional, cylindrical

geometry version of a set commonly used in multifield computational hydrodynamics, originally derived from the general field equations of Ishii.[21,22] A "field," in the context of multifield hydrodynamics, is represented by separate momentum, mass continuity, and energy equations; these three equations are solved for each "field." Mass, energy, and momentum transfer between fields is represented by coupling terms in the field equations, for which constitutive relations must be provided. Also necessary is an equation of state for each field. The field equations, associated constitutive relations, equations of state, and initial and boundary conditions, are solved by use of the SETS, or Stability-Enhancing-Two-Step method, developed by Mahaffy.[18]

The field equations used are:

Mass Continuity:

$$\frac{\partial}{\partial t}(\alpha_k \rho_k) + \nabla\cdot(\alpha_k \rho_k \vec{v}_k) - \Gamma_{jk} - \Gamma_{wk} = 0 \tag{4.1}$$

$$\frac{\partial}{\partial t}(\alpha_1 \rho_h) + \nabla\cdot(\alpha_1 \rho_h \vec{v}_1) - \Gamma_h = 0 \quad , \tag{4.2}$$

Momentum:

$$\frac{\partial}{\partial t} v_{xk} + \vec{v}_k\cdot\nabla v_{xk} + \frac{1}{\rho_k}\frac{\partial P}{\partial x} + \frac{1}{(\alpha\rho)_k}\left[\sum_{j=1}^{4} C_{xjk}(v_{xk} - v_{xj})|v_{xk} - v_{xj}| + C_{xwk} v_{xk}|v_{xk}| + F^{v}_{xk}\right] + g_x = 0 \tag{4.3}$$

(the subscript x represents either the axial or radial direction).
Energy:

$$\frac{\partial}{\partial t}(\alpha_k \rho_k e_k) + \nabla\cdot(\alpha_k \rho_k e_k \vec{v}_k) + P\left(\frac{\partial \alpha_k}{\partial t} + \nabla\cdot\alpha_k \vec{v}_k\right) - \sum_{j=1}^{4} \Gamma_{jk} H_k - \sum_{j=1}^{4} Q_{jk} - Q_{wk} - Q_{sk} = 0 \quad . \tag{4.4}$$

Finally, a constraint on the sum of the fluid volume fractions is required:

$$1 - \sum_{j=1}^{4} \alpha_j - \alpha_s = 0 \quad . \tag{4.5}$$

In the above equations, α_k is the volume fraction with respect to the total finite difference mesh cell volume. There can also be a non-flow volume fraction in the cell, such as fuel pins or structures, α_s. The velocity vector $\vec{v}_k$ is composed of axial and radial components v_{zk} and v_{rk}. The third and fourth terms in Eq.(4.1) represent mass transfer among the fields and external mass source terms, respectively. The mass transfer between steam and liquid water is treated implicitly in temperature and pressure, while the other mass transfers are explicit sources from, for instance, melting fuel pins or steel structures. In the hydrogen mass equation (4.2), the hydrogen is convected with the velocity of the combined vapor field (field 1). The mass source term Γ_h is produced by

oxidation of both structural components, such as fuel pin cladding, and metallic melt components. In the momentum equations (4.3), the fourth term represents momentum transfer between the fields, the fifth term represents wall friction, and the sixth term F^v is the virtual mass force. The coefficients C are evaluated explicitly based on the local flow regime. In the energy equation (4.4), the third term is the work term, the fourth term represents energy exchange between the fields due to phase change, with H_k representing the saturation enthalpy, the fifth term represents heat transfer between fields, the sixth term represents external energy sources, and the seventh term is energy transfer to an interface at saturation.

Equations 4.1 through 4.5 are a set of eighteen coupled, non-linear, partial differential equations that, along with material equations of state and constitutive relations for mass, energy and momentum exchange, form the hydrodynamic equation set in IFCI.

The equation of state used for water-steam is the TRAC equation of state,[20] which consists of analytic fits to the steam tables. Hydrogen and other noncondensible gases are described by the ideal gas law. A stiffened gas equation is used to provide the dependence of melt density on pressure (a crude approximation, but adequate for the present problem):

$$\rho_4 = \frac{1}{a^2} P + \rho_4^* \quad . \tag{4.6}$$

The interfield heat transfer terms in (4.4) are given as

$$Q_{jk} = A_{jk} h_{jk} (T_k - T_j) \quad , \tag{4.7}$$

where the interfacial area per unit volume between fields j and k, A_{jk}, and the heat transfer coefficient, h_{jk}, are provided by constitutive relations for each flow regime.

Mass transfer between the water and steam fields is described by a simple bulk boiling model assuming the existence of an interface between the two fields at the saturation temperature:

$$\Gamma_{12} = A_{12} \frac{h_{2s}(T_2 - T_s) - h_{1s}(T_1 - T_s)}{H_{lg}} \quad . \tag{4.8}$$

Surface boiling at the melt surface is modeled by a subcooled surface boiling model,

$$\Gamma_4 = A_4 \frac{h_{4s}(T_4 - T_s) - h^c_{2s}(T_s - T_2)}{H'_{lg}} \quad , \tag{4.9}$$

where H'_{lg} is an effective latent heat of vaporization, modified to account for the sensible heat of the vapor. Eq. (4.9) is used to describe film boiling at a surface with either saturated or subcooled coolant.

The virtual mass term F^v appearing in Eq. (4.3) is used to add stability to the multifield equations. The form used here is simplified from the full virtual

mass expression as suggested in Bohl et al.[23] and is applied only to discrete vapor flows. The simplified expression for the virtual mass force for the vapor field is

$$F^{v}_{x1} = \alpha_1 \bar{\rho}_L C_{vm} \left[\frac{\partial v_{x1}}{\partial t} - \bar{\alpha}_2 \frac{\partial v_{x2}}{\partial t} - \bar{\alpha}_3 \frac{\partial v_{x3}}{\partial t} - \bar{\alpha}_4 \frac{\partial v_{x4}}{\partial t} \right] , \tag{4.10}$$

where $\bar{\rho}_L$ is an effective liquid density for the water, melt and solid fields, $\bar{\alpha}_k$ is a normalized liquid field volume fraction, and the virtual mass coefficient C_{vm} is set to a value giving stability to the equation set,[24]

$$C_{vm} = 4 \sqrt{\bar{\alpha}_1^3 \, \bar{\alpha}_L \rho_1 / \bar{\rho}_L} \quad . \tag{4.11}$$

4.3 Constitutive Relations

Constitutive relations are provided in IFCI for heat and momentum transfer in the bubbly, slug, and mist flow regimes between water and vapor. Flow regimes for the melt field are derived by treating the water and vapor together as a second phase; the melt is then described, based on the melt volume fraction, as either continuous with entrained vapor-water droplets, or as melt droplets in a continuous vapor-water phase. Provision is also made for the existence of mixture levels, i.e., formation of pools of water or melt.

Heat transfer coefficients (HTCs) between melt and water fields are provided via a boiling curve, which describes nucleate, transition, and film boiling (in the present problem, only the film boiling regime occurs). At high vapor volume fractions, a transition is made between film boiling heat transfer to water and convective heat transfer to vapor from the melt.

4.3.1 Interfacial Friction Coefficients

The drag coefficients C_{jk} between fields j and k are written as

$$C_{jk} = \frac{3}{4} \rho_f \alpha_d \frac{C_f}{D} \quad , \tag{4.12}$$

where the subscripts f and d refer to the continuous fluid and discrete fields, respectively. The friction factor C_f is given by[25]

$$C = \begin{cases} \dfrac{24}{Re} & , \quad Re < 2 \\ \dfrac{18.7}{Re^{0.68}} & , \quad Re \geq 2 \end{cases} \tag{4.13}$$

where the Reynolds number Re is based on the continuous field properties ρ_f and μ_f, the relative velocity v_r, and the characteristic diameter of the discrete field D. The diameter D appearing in Eq. (4.12) is based on a critical Weber number,

$$D = \frac{We_c \sigma}{\rho_f v_r^2} \quad , \tag{4.14}$$

where We_c is 7.5 for bubbles, 4 for droplets of water, and 12 for melt or water-vapor (combined field) drops.[26] If a mixture level is present, then D is the axial hydraulic diameter. For melt, if the melt diameter is larger than the cell size, then a flat interface geometry is assumed and the melt size D_m is used for D.

4.3.2 Interfacial Areas

The interfacial area is calculated as

$$A_{jk} = \frac{6\alpha_d}{D} \quad , \tag{4.15}$$

if a discrete-continuous geometry is present, or the axial area of the cell divided by the cell volume, if the fields are stratified.

4.3.3 Heat Transfer Coefficients

Although there are many heat transfer coefficients provided in the IFCI constitutive relation routines corresponding to the many possible flow conditions, to save space, only those relevant to the present problem will be described, notably those associated with the bulk boiling and surface film boiling conditions. For bulk phase change, the heat transfer coefficients depend on whether the flow regime is bubbly, slug, or mist. The vapor-saturated-interface heat transfer coefficient is

$$h_{1s} = \begin{cases} 1000, & \alpha \le 0.3 \\ \text{slug}, & 0.3 < \alpha \le 0.5 \\ \text{transition}, & 0.5 < \alpha \le 0.75 \\ Nu \ \frac{k_v}{D} \ , & 0.75 < \alpha \le 1 \end{cases} \tag{4.16}$$

The number Nu appearing in Eq. (4.16) is a sphere convection number[27]

$$Nu = 2 + 0.74 \sqrt{Re} \quad . \tag{4.17}$$

The water-saturated interface HTC is

$$h_{2s} = \begin{cases} Nu_l \ \frac{k_l}{D} \ , & \alpha \le 0.3 \\ \text{slug}, & 0.3 < \alpha \le 0.5 \\ \text{transition}, & 0.5 < \alpha \le 0.75 \\ .02 \ \rho_l C_v v_r \ , & 0.75 < \alpha \le 1 \end{cases} \tag{4.18}$$

In the above expression for h_{2s}, the Nusselt number Nu_l is the greater of a sphere forced convection Nusselt number or one derived from the Plesset-Zwick bubble growth formula,[28]

$$Nu = \frac{12}{\pi} \Delta T_{sub} \left[\frac{\rho_l (\partial e_l / \partial T_l)}{\rho_v H_{lg}} \right] \quad . \tag{4.19}$$

The formula for $\alpha > 0.75$ is derived assuming that $Pr = 1$ and $C_v = C_p$.

4.3.4 Film Boiling

The film boiling HTC for the melt is given as

$$h_{4s} = \max\{ h_{free}, h_{force} \} + h_{rad} \quad , \tag{4.20}$$

where the h_{free} and h_{force} are subcooled boiling correlations from Dhir and Purohit,[29]

$$h_{free} = h_{sat} + h_{nat} \frac{\Delta T_{sub}}{\Delta T_w} \quad , \tag{4.21}$$

where h_{sat} is given by the Bromley correlation,

$$h_{sat} = 0.8 \left\{ \frac{g \rho_v (\rho_l - \rho_v) H_{lg} k_v^3}{\mu_v D \Delta T_w} \right\}^{1/4} \quad , \tag{4.22}$$

and h_{nat} is a natural convection correlation

$$h_{nat} = 0.9 \left\{ \frac{g \rho_l^2 C_{pl} \beta \Delta T_{sub} k_l^3}{D \mu_l} \right\}^{1/4} \quad . \tag{4.23}$$

h_{force} is a combination of a saturated boiling HTC h_{sat} and a forced convection HTC,

$$h_{force} = h_{sat} + 0.8 \sqrt{Re} \left(1 + \frac{k_l}{k_v} \frac{\Delta T_{sub}}{\Delta T_w} \right) \frac{k_l}{D} \quad . \tag{4.24}$$

The HTC for convection from the film interface to the bulk liquid water is given by the greater of a natural convection HTC or a forced convection HTC,[25]

$$h_{2s}^c = \max\{ Nu_{nc}, Nu_{fc} \} \frac{k_l}{D} \quad , \tag{4.25}$$

where

$$\begin{aligned} Nu_{nc} &= 2.0 + 0.6 \, Gr^{1/4} Pr^{1/3} \quad , \\ Nu_{fc} &= 2.0 + 0.6 \, Re^{1/2} Pr^{1/3} \quad . \end{aligned} \tag{4.26}$$

Heat transfer from the melt to the vapor in film boiling is derived from the amount of heat given to the vapor as sensible heat in the expression for H'_{lg} as

$$h_{14} = \frac{\Gamma_4}{\Delta T_v} \left(0.1 \, C_{pv} \Delta T_v \right) \quad . \tag{4.27}$$

The radiation HTC h_{rad} is given as

$$h_{rad} = \sigma \epsilon \frac{(T_4^4 - T_2^4)}{(T_4 - T_2)} \quad . \tag{4.28}$$

4.4 Fragmentation Model

The idea of a dynamic fragmentation model, which calculates the characteristic melt diameter as a function of instantaneous hydrodynamic conditions, was first proposed by Camp in Reference 30. A model using this idea was later incorporated into a version of the TEXAS[31] one-dimensional FCI code by Chu and Corradini,[14] using an empirical correlation derived from data obtained in the FITS experiments. The fragmentation model in IFCI is a version of a dynamic fragmentation model developed by Pilch[32] based on Rayleigh-Taylor instability theory and the existing body of gas-liquid and liquid-liquid drop breakup data.

The basic Pilch model describes primary breakup of a drop via penetration of the drop by Rayleigh-Taylor waves, and is expressed as

$$\frac{dD}{dt} = - \frac{(1 - N^{-\frac{1}{3}})}{T^+} |v_r| \epsilon^{\frac{1}{2}} \quad , \tag{4.29}$$

This formulation was developed from the observation that, in high Weber number drop breakup experiments, the drop experiences primary breakup into 3-5 primary fragments in a dimensionless time T^+ of 1-1.25. While primary breakup is occurring, smaller fingers continuously develop and break off, forming a cloud of droplets; this effect is included via a surface entrainment model, given as

$$\frac{dS}{dt} = C_0 C_f^{\frac{3}{4}} \frac{1}{D} We^{\frac{1}{4}} |v_r| \epsilon^{\frac{1}{2}} \quad , \tag{4.30}$$

where C_0 is a constant $\simeq$ 0.089. A detailed derivation and comparison to experiment of the fragmentation model can be found in Reference 33.

The drop breakup data from which (4.29) and (4.30) were derived consisted of isothermal liquid-gas and liquid-liquid breakup data. It is assumed here that this correlation will also apply under boiling conditions; there is some justification for this assumption in the experiments of Greene et al,[34] in that the drag coefficients for heated (boiling) and isothermal (nonboiling) steel balls dropped into water were about the same. The drag coefficient enters into (4.29-4.30) through the Bond-Weber number equivalence; since the drag coefficient is essentially unchanged, the model is assumed to hold for both boiling and isothermal systems. A more important effect of boiling on the overall breakup is to cause higher local relative velocities and pressure fluctuations, accelerating the breakup process, as will be seen in a later section.

In IFCI, a drop is described by an Eulerian melt field, interacting with the other three fields, also Eulerian. The fuel mass may either be smaller than a finite difference mesh cell (subgrid size) or extend over many cells; in the former case, the fuel melt exists as discrete drops and the primary breakup formulation is applicable, along with surface entrainment; in the latter case, surface area generation takes place as the melt geometry distorts due to hydrodynamic motion on the finite difference grid; in addition, the surface entrainment subgrid fragmentation model is used in cells containing a melt-water interface.

In IFCI, the fragmentation mechanisms described by Eqs. (4.29-4.30) are expressed in terms of rate of change of surface area per unit cell volume, as this is the convected quantity (Ishii,[21] p.179). This surface area formulation allows treatment of jets and other more general flows, as well as drops. The conversion to volumetric surface area generation rate requires knowledge of the relation between volumetric surface area A_m and characteristic diameter D; in the case of discrete drops, this is given by

$$A_m = \frac{6\alpha_m}{D} \quad . \tag{4.31}$$

Differentiating the expression for volumetric surface area leads to an equation for rate of change of A_m in terms of the rate of change of diameter for the primary breakup model, Eq. (4.29):

$$\Gamma_p = \frac{dA_m}{dt} = - \frac{6\alpha_m}{D^2} \frac{dD}{dt} = - A_m \frac{1}{D} \frac{dD}{dt} \ , \tag{4.32}$$

where Γ_p = surface area source due to primary breakup (m^2/m^3-s). In the case of the surface entrainment rate per unit melt area dS/dt, simply multiplying this rate by the volumetric melt area A_m gives the volumetric entrainment rate Γ_e. These surface generation rates are used as surface area source terms in the continuity equation for A_m, written as

$$\frac{\partial A_m}{\partial t} + \nabla \cdot (v_m A_m) = \Gamma_p + \Gamma_e \quad . \tag{4.33}$$

After solving the surface area transport Eq. (4.33) for a timestep, new values of the characteristic melt diameter are calculated from the new surface area by the reverse procedure. The present formulation of the surface area transport allows only one melt characteristic diameter per cell, which is assumed to represent a mean value of the actual size distribution in the cell.

A surface tracking algorithm is used to account for surface area generated by distortion of the fuel mass from its initial geometry due to hydrodynamic motion. This is necessary because the fragmentation rate mechanisms Eqs. (4.29-4.30) are both subgrid-scale models that do not account for large-scale distortions; they depend, however, on the characteristic size D, which can change if, for instance, a fuel mass initially in a single spherical drop distorts into a hollow sphere. The surface tracking algorithm is loosely based on that used in the Volume-Of-Fluid method,[35] except that the primary purpose here is to find the local characteristic diameter, and tracking the interface is a necessary step rather than the final result.

5 FCI Example Problem

The initial test problem for the IFCI code has been used both as a demonstration of the capabilities of IFCI and to detect problems in the numerics and/or phenomenological models. The test problem is a simulation of a representative FITS experiment, using typical experiment conditions as the initial and boundary conditions for IFCI. The first case, RUN1, used only the primary fragmentation model and the saturated bulk boiling model. RUN4A, the second case, used the surface entrainment model, surface tracking algorithm, and subcooled boiling model also. RUN6 is an isothermal case in which the melt is at the same temperature as the water.

The following sections describe the setup of the problem on the IFCI computational mesh, the results of the coarse mixing phase, and the results of the triggering and propagation phase for RUN1. Calculation of the expansion phase was not carried out to its conclusion, as the main purpose of the test calculation was to test the operation of IFCI during the coarse mixing and propagation phases. The coarse mixing phase was repeated in cases RUN4A and RUN6.

5.1 Problem Setup

The problem conditions are patterned after the FITS "D" medium scale pouring mode experiments.[7] In these experiments, roughly 20 kg of molten iron-alumina generated by a thermite reaction was dropped into water 15-66 cm deep contained in a square Plexiglas tank. The velocity of the melt on entry into the water was 5.7-7.3 m/s. Water temperature ranged from 284 K to 368 K, and pressure varied from 0.085 MPa to 1.1 MPa.

The problem was set up in IFCI's R-Z geometry using 5 radial nodes and 10 axial nodes (see Figure 1); although this mesh is fairly coarse, it is adequate for preliminary testing of the code. The water chamber is approximated as a cylinder 61 cm high by 69 cm in diameter; the cross-sectional area is thus the same as the square Plexiglas chamber in many of the FITS D series tests. The initial water temperature was 373 K, or saturation temperature at 0.1 MPa pressure. The initial melt temperature was 2700 K, and an entrance velocity of 5.9 m/s was used. The initial melt configuration was approximated as a cylinder 20 cm in diameter and 21 cm long, with a total melt mass of 25 kg.

Figure 1 shows the initial position of the melt and water on the problem grid. As shown, the tail of the melt enters the top edge of the problem grid through an inlet boundary condition applied at the top two innermost nodes. An outlet pressure boundary condition is applied on the outside axial edge of the top outermost node. All other boundaries are fixed, which means, in terms of experiment simulation, that pressures generated during the propagation phase of the FCI will not be relieved as in the experimental Plexiglas chamber (essentially a free boundary). The calculation is started at the time of initial melt-water contact.

5.2 Coarse Mixing Phase

In the coarse mixing phase of the problem, the melt enters the water and falls to the bottom of the water chamber. Heat transfer between the hot melt and the surrounding water is limited by film boiling. The melt fragments and

mixes with the surrounding water-steam mixture, spreading out radially as it falls. Experimentally, a roughly paraboloid shape for the coarse-mixing region (Figure 2) is observed.

A contour plot of the macroscopic melt density ($\alpha\rho$) is shown at the end of the fall phase for RUN1, 0.3 s, in Figure 3. An interesting feature is the appearance of a steam-water chimney in the interior of the mixture region, which can be seen in Figure 3 and Figure 4, the vapor volume fraction at 0.3 s. The axial average steam volume fraction in the chimney at this time is around 0.25. Comparing Figures 3 and 4, it is apparent that most of the vapor generation is occurring above (behind) the main melt mass. This is due to the saturated bulk boiling model and the hydrostatic pressure head in the tank, as can be seen in the comparison calculation using the subcooled boiling model.

In RUN4A, the subcooled boiling model, surface entrainment model, and surface tracking were used. The melt distribution at time of bottom contact for this case is shown in Figure 5, where it is apparent that the overall mixture region is considerably larger than in RUN1. The time of bottom contact is also later, 0.4 s versus 0.3 s. A steam chimney is still present, but steam is now being generated near the main melt mass at the tank bottom, Figure 6.

A comparison case (RUN6) using isothermal melt at 373 K was done to examine the effect of boiling on mixing and fragmentation. The melt distribution at 0.4 s for this case is shown in Figure 7; there is much less dispersal for this case than for the boiling cases, and the melt is in a single mass rather than spread in a paraboloid. The degree of melt spreading in RUN6 appears comparable to that observed for isothermal freon-water jet experiments,[36] although it is hard to tell from the coarse grid in the present calculation.

The water/melt mass ratio in the mixture region is an important parameter for characterizing FCI mixtures, as the maximum theoretical thermodynamic efficiency goes through a peak as the water/melt ratio is varied. The peak occurs at a ratio of about 0.5 for thermite/water mixtures at atmospheric pressure. The ratio in RUN1 at 0.3 s, calculated as the fuel-mass-weighted mean, is 1.1, which is slightly below the peak on the efficiency curve. The mean water/melt mass ratios for RUN4A and RUN6 are 4.2 and 1.2, respectively; the former ratio, 4.2, represents a very water-rich mixture with a peak thermodynamic efficiency of 0.1, versus the peak of 0.3.

Another parameter used to assess mixing is the steam volume fraction in the mixture region. The usual experimental procedure for the FITS experiments was to either use measurements of water level swell to estimate the steam volume fraction in the entire tank, which was then assumed to be confined to the mixture region, or, for some tests,[9] the volume of the mixture region was estimated from the mixture region outline as seen on the photographic records, and, assuming a homogeneous mixture region (ie, neglecting any possible steam chimney or other spatial variation of the mixture), the average void fraction in the mixture region could be obtained.

In RUN1, estimating the mixture volume from the mixture outline in Figure 3 gives 0.38 for the average steam fraction and 0.66 for the average water/melt mass ratio. The mean steam volume fraction in the actual mixture region for the test problem (obtained by weighting the cell steam volume fractions

by the cell melt masses) is 0.065, which is quite different from the values obtained assuming that the mixture region is homogeneous. The difference is caused by the neglect of the spatial variation of the mixture components (most of the vapor is contained in the vapor chimney) and by the delay in boiling as the melt falls through the water, causing the vapor to trail the melt. The mixture region vapor volume fraction in RUN4A is 0.5, versus 0.065 in RUN1.

The Sauter and median melt-mass diameters for RUN1 decreased during the fall from an initial value of 20 cm to a value of 15 cm at 0.3 s, and showed very little spatial variation. This coarse mixing diameter is quite large compared to experimental measurements of final debris sizes of ~1 cm. The calculated diameter is also at variance with the apparent characteristic size, as determined by examining the melt spatial distribution in Figure 3: the distribution would suggest a melt size closer to 5-10 cm. The main reason for this discrepancy is that the surface generation source in the transport equation does not account for the effect of surface generation by large-scale hydrodynamic motion of the melt. In the present problem, the melt distorts from an initial cylindrical shape into a hollow paraboloid or conic shape in the presence of boiling. Use of the surface tracking algorithm corrects this problem, as will be seen in the discussion of particle size distributions from the three cases.

5.3 Triggering and Propagation Phase

To simulate the triggering and propagation phase, a local explosion was artificially triggered at 0.3 s. The trigger was simulated by introducing a large surface area source in the bottom innermost node of the problem, which decreased the characteristic diameter of the melt in this "trigger cell" from 15 cm to 100 μm over a time period of 500 μs. The final melt diameter was chosen as typical of observed debris sizes after an explosive FCI, and the time period over which fragmentation occurs was based on observed propagation speeds and reaction zone lengths from FITS tests, but is strictly an estimated number.

The pressure pulse resulting from the trigger reached a maximum of about 10 MPa in the trigger and neighboring cells, typical of trigger pressures acheived by the detonators used in the FITS experiments. This level of pressure induced sufficient relative velocity (10-20 m/s) to cause fine fragmentation down to sizes of 100 μm along the problem center axis. No steady-state propagation was observed. The pressure and induced relative velocity died away fairly rapidly with increasing radius, resulting in a decrease in fragmentation with radius and consequent larger final melt diameter. The melt diameter was around 100 μm on the center axis, increasing to around 1-4 mm at the outside of the melt region; these larger sizes were in cells that also contained the bulk of the melt, resulting in an overall small transfer of heat from the melt to the water over the timescale of the propagation. The relatively low degree of fragmentation in RUN1 suggests that mixing conditions in RUN1 were not optimum for a propagating detonation to occur, or that the nodalization used was too coarse to resolve the pressure peak in a propagating shock calculation.

The time at which the propagation phase ended was taken as the time at which the cell farthest from the trigger point containing significant melt mass showed a rapid decrease in melt diameter; this occurred at 0.31 s on the water

surface. The speed of propagation varied with local three-phase mixture conditions, ranging from 270 m/s close to the trigger cell (a region containing mostly melt and water) down to 60 m/s at the top of the steam chimney (a region containing mostly vapor). During pressure propagation, the pressure behind the advancing pressure front was around 2.5 MPa, about one-quarter the magnitude of the initial trigger pulse. This overpressure was sufficient, however, to partially collapse the steam chimney above the melt (see Figure 8).

An estimate of thermal conversion efficiency can be made by dividing the kinetic energy of the system by the total energy in the melt.[37] Using a specific energy of 2.8 MJ/kg as the thermite melt energy content,[5] the initial melt mass of 25 kg, and the kinetic energy of the system at 0.31 s, we get a thermal-energy-to-work conversion ratio of 0.03%, which would be considered as a steam spike rather than an explosion, experimentally. Considering only the thermal energy between melt initial temperature and the freezing point (around 1850 K) raises this conversion ratio to 0.1%.

5.4 Melt Size Distributions

The melt size distribution was derived at the end of the coarse mixing and propagation phases by binning the melt mass and diameter in each cell into size ranges corresponding to standard sieve sizes, normalizing with the total melt mass, and dividing by the size range for each bin.[38]

The size distribution function for the propagation phase (RUN1) is shown in Figure 9, along with the debris distribution from the FITS0D test, an experiment which did not explode, but did have a surface "eruption."[7] Since the results of RUN1 do not seem to represent a strong FCI, this comparison is more applicable than comparing to a test with a strong explosion.

The distributions in Figure 9 match fairly well, although some of the smaller sizes are absent from the RUN1 results. The peak in the RUN1 distribution at 100 μm is probably from the trigger event, a judgment supported by noting that the amount of mass represented by the peak (sizes below 212 μm) is 1% of the total melt mass, compared to the melt mass contained in the trigger cell, 2%. The rest of the sizes are in a fairly flat distribution from 300 μm to 2.5 mm. The peak in the FITS0D data in the largest bin (2.5 cm and larger), which is not present in RUN1, probably means that the main pressure event in RUN1 (a trigger at the bottom) did a better job of fragmenting the melt than the main pressure event in FITS0D (an eruption at the water surface).

Figure 10 shows the cumulative melt mass versus melt particle size for FITS0D, RUN1, RUN4A, and RUN6 at the end of coarse mixing. The RUN4A distribution matches the experimental data very well; the reduction in the larger sizes present is due to the surface tracking algorithm, and the sizes under around 5-7 cm are generated by the fragmentation model.

Also derived were two length scales used to characterize debris experimentally, the Sauter mean diameter and the mass median.[38] These two length scales are shown in Table 1 for the FITS "D" series and the three calculated cases. The diameters from the propagation phase of RUN1 (SE, steam explosion) are similar to those from the FITS non-exploding experiments which had an eruption, whereas the RUN1 coarse mixing diameters (BC, bottom contact) are ten times

larger than those in the non-exploding FITS2D experiment. The RUN1 BC mass median diameter, in fact, is 50% larger than the RUN6 isothermal result, due to the lack of surface tracking in RUN1. RUN4A Sauter and mass median diameters are both very close to the non-exploding FITS2D, which has a Sauter mean twice those that "erupted," and (probably more significantly) a mass median four times those that erupted. The single steam explosion experiment, FITS5D, has both a Sauter mean and mass median ten times smaller than those with eruptions.

6 Discussion and Conclusions

The results of this series of test calculations with IFCI are very encouraging to the eventual goal of predicting FCI effects at reactor scale. Observed experimental characteristics, such as the overall shape of the mixture region as the melt falls through the water and the propagation speed of the pressure front through the melt, are seen in the calculations. The important parameters used to characterize FCIs were obtained from the calculations, namely water/melt mass ratio, vapor volume fraction, particle size distribution, and thermal-energy-to-work conversion efficiency. Coarse mixing melt drop sizes from RUN4A are close to experimental coarse mixing debris data, and serve as a semi-validation of IFCI fragmentation models. The results are only a semi-validation because the test problem is a generic pouring mode problem, not a specific experiment. It is hoped that calculation of a specific, well-characterized FITS test will be done in the near future.

The effect of boiling on mixing was observed between RUN1, RUN4A, and RUN6; in the boiling case, both degree of fragmentation and dispersal were significantly larger than in the isothermal case. In both boiling cases, the melt distorted from its initial compact shape into a hollow paraboloid shape enclosing a steam chimney, whereas in the isothermal case, the melt remained essentially in a single mass.

A point of interest is the high water/melt mass ratio calculated in RUN4A; this result suggests that the mixing geometry in the pouring mode FITS tests may have resulted in fairly water-rich mixtures, far from the thermodynamic optimum water/melt mass ratio.

It appears to the author that the global parameters obtained for the mixture region, namely the Sauter diameter (from which total surface area of the melt can be found), the water/melt mass ratio, and the vapor volume fraction, form a sufficient set of parameters to characterize a coarse mixture. Further analysis on the detonability of mixtures should then allow a definition of what combination of coarse mixture parameters can lead to a propagating FCI.

It should be noted that many of the parameters available from IFCI calculations are difficult to observe experimentally; for instance, the the actual water/melt mass ratio in the mixture region requires determination of the spatial distribution of the three-phase system. Another example is the calculation of a steam chimney forming in the mixture region, which has not been observed directly in experiments, although its presence has been suggested. It appears important to somehow measure the spatial variation of the three-phase mixture experimentally, both to verify the calculational results and to accurately determine the characteristics of the actual mixture region.

The present calculation represents a first attempt at simulating the complete FCI process in two dimensions, including dynamic fragmentation, boiling, and interfield slip; these features all appear necessary to correctly simulate FCIs.

Essentially all models necessary to simulate the coarse mixing phase are in IFCI (at least in principle). The remaining models to be included are a metal oxidation model and a fine fragmentation model for use in the propagation phase that includes the effect of water penetration and entrapment by melt.[2,4,39]

The next major validation tests envisioned for IFCI are a coarse mixing calculation of a specific FITS pouring mode experiment and a calculation of a jet mixing mode experiment, probably using the IJET and EJET[36] tests. These calculations will serve as validation that the IFCI models, previously tested individually against separate-effects experiments, are correctly simulating mixing in medium-scale experiments. This validation is a crucial step in the eventual use of IFCI to calculate FCI effects at large scale in a reactor accident scenario.

7 References

1. M. F. Young, "IFCI: An Integrated Code for Calculation of All Phases of Fuel-Coolant Interactions," SAND87-1048, NUREG/CR-5084, Albuquerque, NM (September 1987).

2. B. Kim, "Heat Transfer and Fluid Flow Aspects of Small-Scale Single Droplet Fuel-Coolant Interactions," PhD Thesis, University of Wisconsin-Madison, WI (1985).

3. M. L. Corradini, "Phenomenological Modeling of the Triggering Phase of Small-Scale Steam Explosion Experiments," Nucl. Sci. & Eng. 78, pp.154-170 (1981).

4. B. Kim and M. L. Corradini, "Modeling of Small-Scale Single Droplet Fuel/Coolant Interactions," Nucl. Sci. & Eng. 98, pp.16-28 (1988).

5. D. E. Mitchell et al, "Intermediate Scale Steam Explosion Phenomena: Experiments and Analysis," SAND81-0124, NUREG/CR-2145, Albuquerque, NM (September 1981).

6. M. L. Corradini, "Analysis and Modelling of Steam Explosion Experiments," SAND80-2131, NUREG/CR-2072, Albuquerque, NM (1981).

7. B. W. Marshall Jr., "Recent Fuel-Coolant Interaction Experiments Conducted in the FITS Vessel," 25th ASME/AIChE National Heat Transfer Conference, Houston, TX (July 1988).

8. W. R. Bohl, "An Investigation of Steam Explosion Loadings with SIMMER-II," draft report, Los Alamos, NM (1986).

9. D. V. Swenson and M. L. Corradini, "Monte Carlo Analysis of LWR Steam Explosions," SAND81-1092, NUREG/CR-2307, Albuquerque, NM (1981).

10. M. G. Stevenson, "Report of the Zion/Indian Point Study," LA-8306-MS, NUREG/CR-1411, Los Alamos, NM (April 1980).

11. S. G. Bankoff and A. Hadid, "The Application of a User-Friendly Code to Nuclear Thermalhydraulic Reactor Safety Problems," Proc. Int. Nuclear Power Plant Thermal Hydraulics and Operations Topl. Mtg., Taipei, Taiwan, American Nuclear Society (1984).

12. M. A. Abolfadl and T. G. Theofanous, "An Assessment of Steam-Explosion-Induced Containment Failure. Part II: Premixing Limits," Nucl. Sci. & Eng. 97, pp.282-295 (1987).

13. A. Thyagaraja and D. F. Fletcher, "Buoyancy-Driven, Transient, Two-Dimensional Thermo-Hydrodynamics of a Melt-Water-Steam Mixture," CLM-P790, UKAEA, Culham Laboratory, Abingdon, UK (1986).

14. C. C. Chu and M. L. Corradini, "One-Dimensional Transient Fluid Model for Fuel/Coolant Interaction Analysis," Nucl. Sci. & Eng. 101, pp.48-71 (1989).

15. C. Carachalios et al, "A Transient Two-Phase Model to Describe Thermal Detonations Based on Hydrodynamic Fragmentation," Proc. Intl Mtg on LWR Severe Accident Evaluation, Cambridge, MA (1983).

16. S. Medhekar et al, "Triggering and Propagation of Steam Explosions," ASME-AICHE Heat Transfer Conf, Houston, TX (1988).

17. D. F. Fletcher and A. Thyagaraja, "Multiphase Detonation Modelling using the CULDESAC Code," 12th Intl. Colloquium on the Dynamics of Explosions and Reactive Systems, Ann Arbor, MI (1989).

18. J. H. Mahaffy, "A Stability-Enhancing Two-Step Method for Fluid Flow Calculations," J. Comp. Phys. 46, p.329 (1982).

19. J. F. Dearing, "A Four-Field Model of PWR Degraded Cores," Third International Topical Meeting on Reactor Thermal-Hydraulics, Newport, RI (October 1985).

20. TRAC-PF1: An Advanced Best-Estimate Computer Program for Pressurized Water Reactor Analysis," LA-9944-MS, NUREG/CR-3567, Los Alamos, NM (1984).

21. M. Ishii, Thermo-Fluid Dynamic Theory of Two-Phase Flow, Eyrolles, France (1975).

22. G. Kocamustafaogullari, "Thermo-Fluid Dynamics of Separated Two-Phase Flow," PhD Thesis, Georgia Inst of Tech, GA (1971).

23. W. R. Bohl et al, "Computational Methods of the Advanced Fluid Dynamics Model," Proc. ANS Mtg. on Advances in Reactor Physics, Mathematics, and Computation, Paris, France (1987).

24. H. C. No and M. S. Kazimi, "Effect of Virtual Mass Effects on the Mathematical Characteristics and Numerical Stability of the Two-Fluid Model", Nucl. Sci. & Eng. 89, pp.197-206 (1985).

25. R. B. Bird et al, Transport Phenomena, John Wiley & Sons (1960).

26. D. R. Liles et al, "TRAC-PF1/MOD1 Correlations and Models," LA-11208-MS, NUREG/CR-5069, Los Alamos, NM (1988).

27. K. Lee and D. J. Ryley, "The Evaporation of Water Droplets in Superheated Steam," ASME 68-HT-11 (1968).

28. B. B. Mikic et al, "On Bubble Growth Rates," Int. J. Heat Mass Transfer 13, pp.657-666 (1970).

29. V. K. Dhir and G. P. Purohit, "Subcooled Film-Boiling Heat Transfer from Spheres," AICHE-ASME Heat Transfer Conf, Salt Lake City, UT (1977).

30. M. F. Young et al, "The FCI Potential of Oxide and Carbide Fuels: Results of the Prompt Burst Series at Sandia Laboratories," Fourth CSNI Specialist Meeting on Fuel-Coolant Interaction in Nuclear Reactor Safety, Bournemouth, UK (April 1979).

31. M. F. Young, "The TEXAS Code for Fuel-Coolant Interaction Analysis," Proceedings of the LMFBR Safety Topical Meeting, Lyon-Ecully, France (July 1982).

32. M. Pilch, "Acceleration Induced Fragmentation of Liquid Drops," PhD Thesis, University of Virginia (1981).

33. M. Pilch and M. F. Young, "Comparison of Dynamic Fragmentation Model to Experiment," to be published.

34. G. A. Greene, T. Ginsberg, N. K. Tutu, "BNL Severe Accident Sequence Experiments and Analysis Program," Proc. Twelfth Water Reactor Safety Research Information Mtg., NUREG/CP-0058, Vol. 3 (1985).

35. B. D. Nichols et al, "SOLA-VOF: A Solution Algorithm for Transient Fluid Flow with Multiple Free Boundaries," LA-8355, Los Alamos, NM (1980).

36. B. W. Marshall, Jr and M. Berman, "An Experimental Study of Isothermal and Boiling Liquid Jets," 14th Water Reactor Safety Research Information Meeting, Gaithersburg, MD (October 1986).

37. D. E. Mitchell and N. A. Evans, "Steam Explosion Experiments at Intermediate Scale: FITSB Series," SAND83-1057, NUREG/CR-3983, Albuquerque, NM (February 1986).

38. A. S. Foust et al, Principles of Unit Operations, 2nd Edition, John Wiley & Sons (1980).

39. L. Nelson et al, "Photographic Evidence for the Mechanism of Fragmentation of a Single Drop of Melt in Triggered Steam Explosion Experiments," Journal of Nonequilibrium Thermodynamics (In Press, 1986).

Table 1
Length Scales from IFCI and FITS "D" Series

TEST	EVENT*	SAUTER MEAN DIAMETER (mm)	MASS MEDIAN DIAMETER (mm)
RUN1	BC (0.3s)	150.	150.
RUN1	SE	1.26	4.0
RUN4A	BC (0.4s)	1.8	12.7
RUN6	BC (0.4s)	25.5	106.0
FITSOD	NE(ER)	1.5	4.6
FITS2D	NE(BC)	3.1	16.0
FITS5D	SE	0.25	0.48
FITS8D	NE(ER)	0.81	3.4

* NE - no explosion SE - steam explosion BC - bottom contact ER - eruption

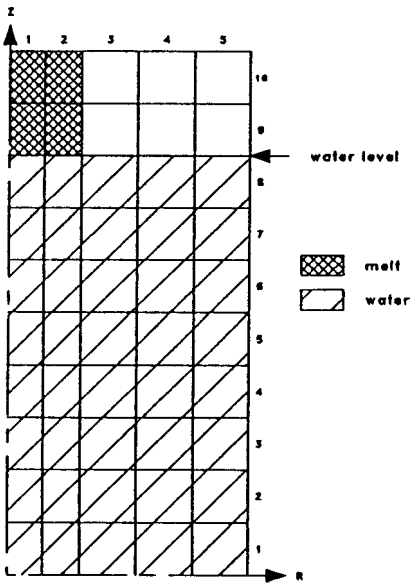

Figure 1. IFCI Test Problem Mesh Setup

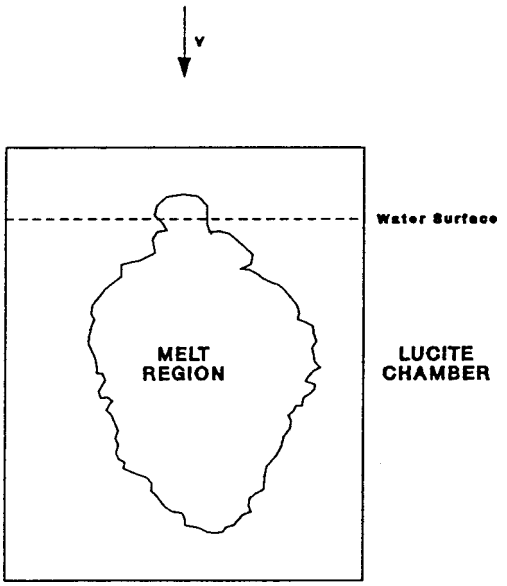

Figure 2. Typical Melt Outline in FITS Experiment

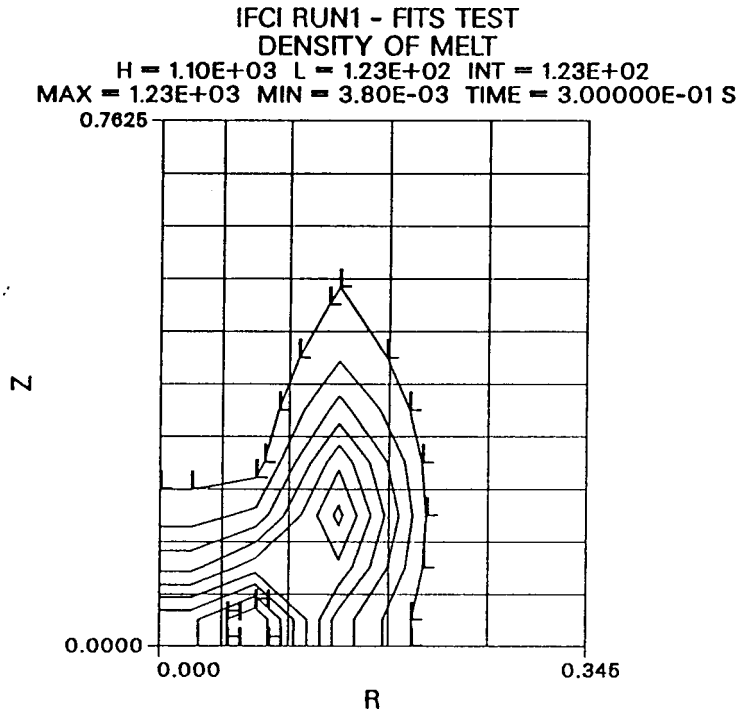

Figure 3. Melt Density at Time 0.3 s in RUN1

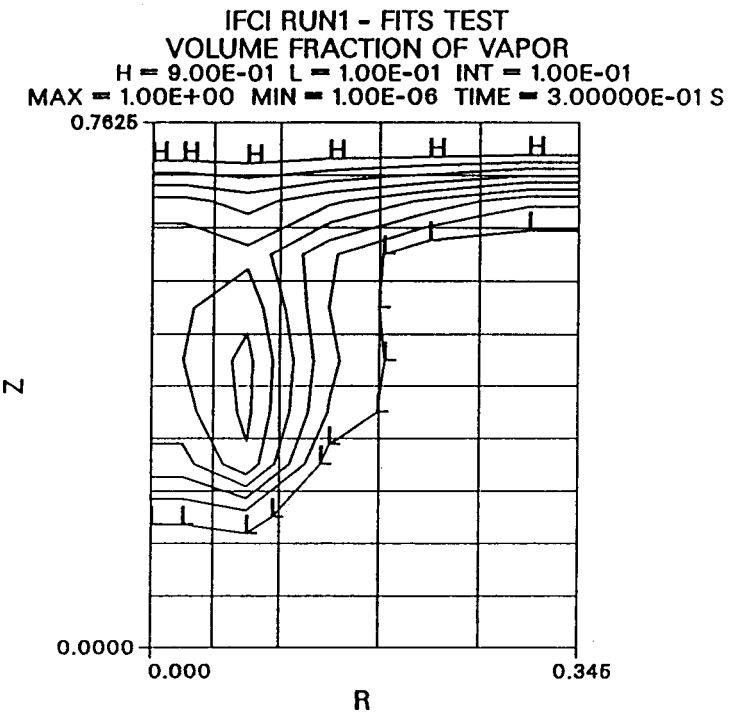

Figure 4. Vapor Volume Fraction at Time 0.3 s in RUN1 Showing Steam Chimney

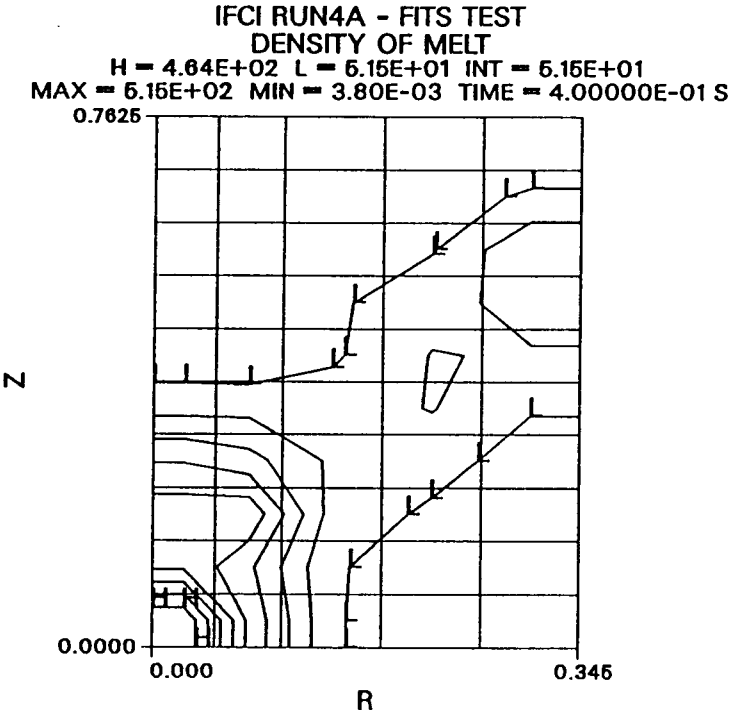

Figure 5. Melt Density at Time 0.4 s in RUN4A

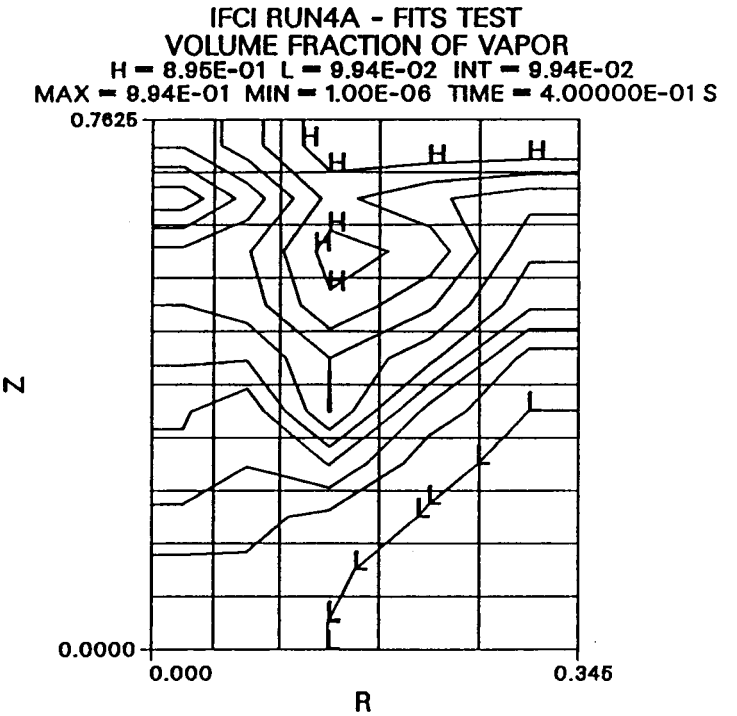

Figure 6. Vapor Volume Fraction at Time 0.4 s in RUN4A Showing Steam Chimney

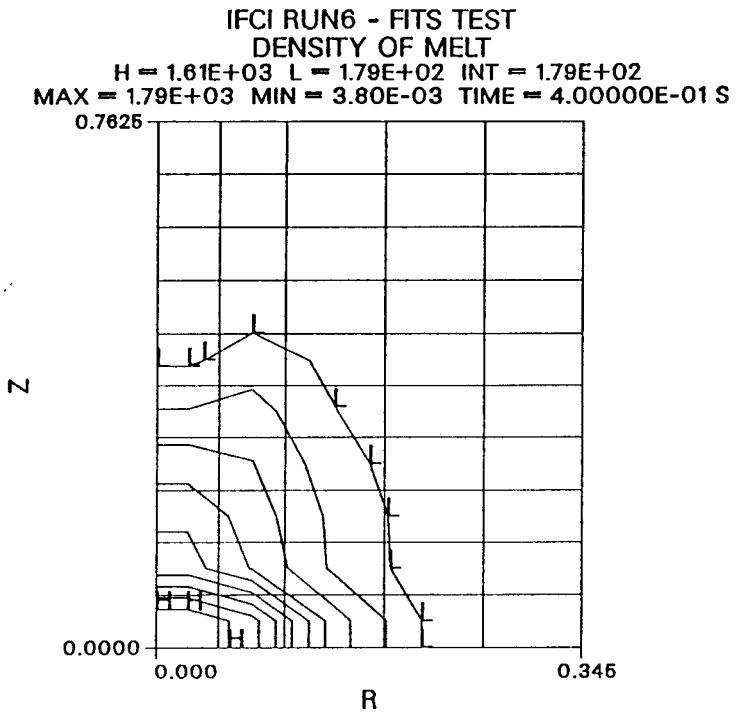

Figure 7. Melt Density at Time 0.4 s in RUN6

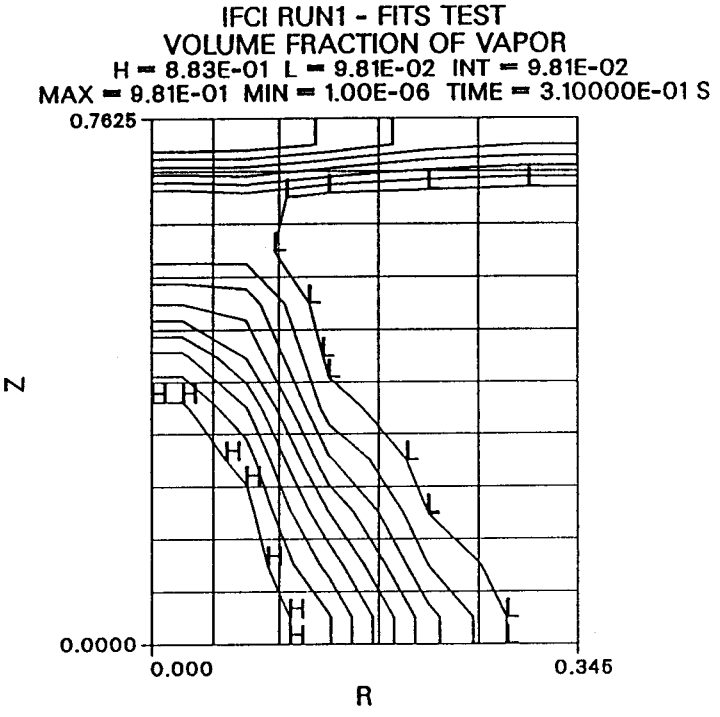

Figure 8. Vapor Volume Fraction at Time 0.31 s in RUN1 Showing Collapse of Steam Chimney

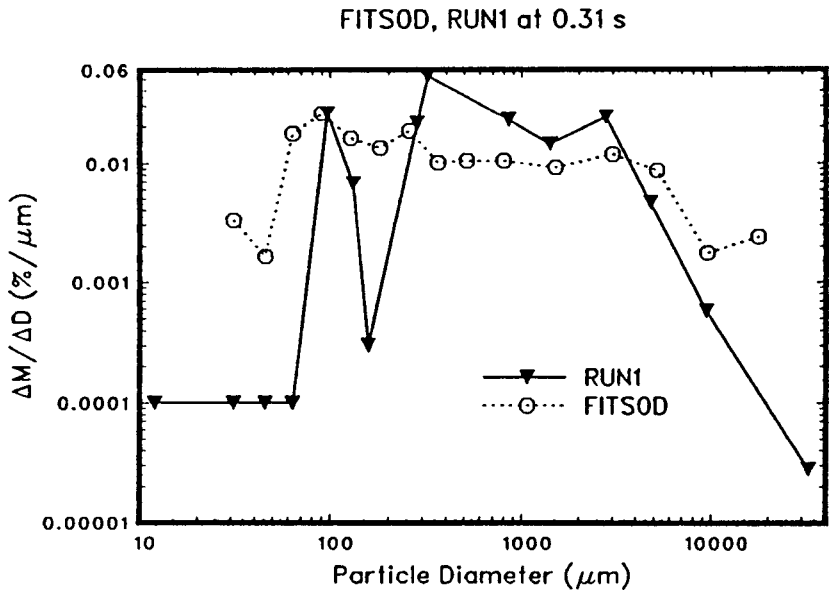

Figure 9. Melt Size Distributions from RUN1 and FITSOD Posttest Debris

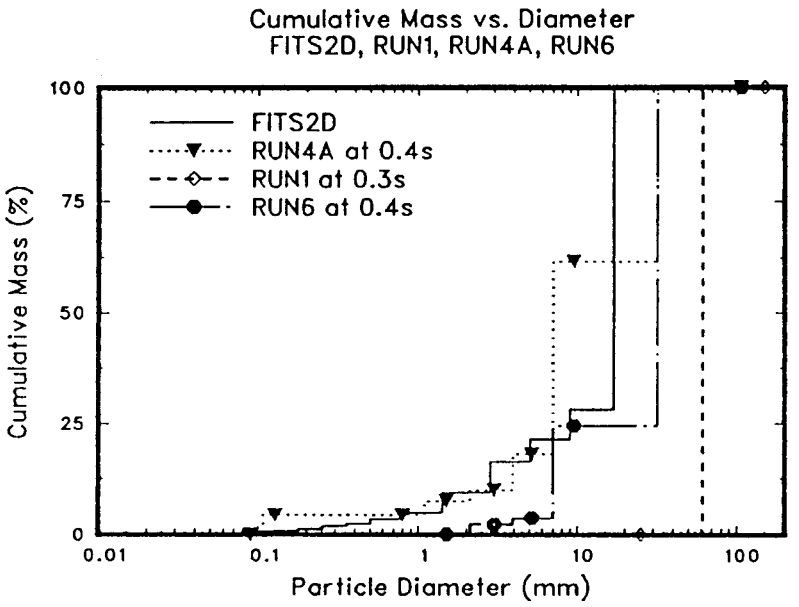

Figure 10. Cumulative Melt Mass versus Melt Diameter for FITS0D and IFCI Cases at End of Coarse Mixing

Glossary

α = Volume fraction,
ρ = density (kg/m^3),
$\mathbf{v}$ = velocity vector (m/s),
v = velocity (m/s),
Γ = mass transfer rate (kg/m^3-s),
Γ_p = primary surface area generation rate (m^2/m^3-s),
Γ_e = entrainment surface area generation rate (m^2/m^3-s),
P = pressure (Pa),
C = drag coefficient ($Pa\text{-}s^2/m^3$),
F^v = virtual mass force (N/m^3),
g = gravitational acceleration (m/s^2).
e = internal energy (J/kg),
H = enthalpy at saturation (J/kg),
Q = energy transfer term (W/m^3),
a = adiabatic sound speed (m/s),
A = interfacial area per unit volume (m^2/m^3),
h = heat transfer coefficient ($W/m^2\text{-}K$),
k = thermal conductivity (W/m-K),
T = temperature (K),
T^+ = dimensionless breakup time = $v_{rel}t/D$,
H_{lg} = latent heat of evaporation (J/kg),
D = drop diameter (m),
t = time (s),
N = number of primary fragments,
ϵ = density ratio = ρ_∞/ρ_d,
Re = Reynolds number = vD/ν,

Gr = Grashof number = $(\beta g \Delta T D^3)/\nu^2$,
Pr = Prandtl number = $C_p \mu/k$,
We = Weber number = $\rho v^2 D/\sigma$,
μ = dynamic viscosity (kg/m-s),
ν = kinematic viscosity (m^2/s),
σ = surface tension (Pa-m) or Stefan-Boltzmann constant,
β = thermal expansion coefficient (K^{-1}),
$\Delta T_w = T_4 - T_s$,
$\Delta T_{sub} = T_s - T_2$,
$\Delta T_v = T_s - T_1$.

Subscripts:

j,k = field 1-4,
1-4 = fields 1 through 4 (vapor, water, melt, solids respectively),
v = vapor,
l = liquid water,
m = melt,
s = structure or saturation,
sub = subcooled,
sat = saturation,
nat = natural convection,
h = hydrogen,
r = radial direction or relative,
z = axial direction,
p = primary,
d = discrete,
f = continuous fluid,
c = critical,
∞ = bulk fluid,
w = wall or structure,
fc = forced convection,
nc = natural convection.

Superscripts:

° = reference quantity,
c = convective.